npj | quantum materials

Article

Published in partnership with Nanjing University

https://doi.org/10.1038/s41535-024-00644-4

Spectral stability of V2 centres in sub-micron 4H-SiC membranes

Check for updates

Jonah Heiler[1,2,3,8], Jonathan Körber[1,8] ✉, Erik Hesselmeier[1,8], Pierre Kuna[1], Rainer Stöhr[1], Philipp Fuchs[4], Misagh Ghezellou[5], Jawad Ul-Hassan[5], Wolfgang Knolle[6], Christoph Becher[4], Florian Kaiser[1,2,3] ✉ & Jörg Wrachtrup[1,7]

Colour centres in silicon carbide emerge as a promising semiconductor quantum technology platform with excellent spin-optical coherences. However, recent efforts towards maximising the photonic efficiency via integration into nanophotonic structures proved to be challenging due to reduced spectral stabilities. Here, we provide a large-scale systematic investigation on silicon vacancy centres in thin silicon carbide membranes with thicknesses down to 0.25 μm. Our membrane fabrication process involves a combination of chemical mechanical polishing, reactive ion etching, and subsequent annealing. This leads to highly reproducible membranes with roughness values of 3–4 Å, as well as negligible surface fluorescence. We find that silicon vacancy centres show close-to lifetime limited optical linewidths with almost no signs of spectral wandering down to membrane thicknesses of ~0.7 μm. For silicon vacancy centres in thinner membranes down to 0.25 μm, we observe spectral wandering, however, optical linewidths remain below 200 MHz, which is compatible with spin-selective excitation schemes. Our work clearly shows that silicon vacancy centres can be integrated into sub-micron silicon carbide membranes, which opens the avenue towards obtaining the necessary improvements in photon extraction efficiency based on nanophotonic structuring.

Optically active spins in solids have implemented quantum technology applications across all fields[1]. Following up on landmark experiments with nitrogen-vacancy (NV) centres in diamond, a current technology trend focuses on colour centres in industrial semiconductor platforms, to benefit from advanced (nano-) manufacturing at the wafer-scale. Recent work identified colour centres and optically active dopants across a variety of semiconductor materials, such as GaN[2,3], AlN[4], ZnO[5,6], Si[7–9], and SiC[10,11]. For the latter two, nuclear spin-free crystals based on isotope purification are already established, which resulted in multi-second colour centre spin coherence times[12]. Additionally, colour centres in SiC have demonstrated nearly lifetime limited optical transitions, which enabled high-fidelity spin-photon interfaces that are suitable for quantum communication[13].

A current issue for quantum applications with individual colour centres concerns the efficient collection of fluorescence photons. The high refractive index of the above-mentioned materials ($n > 2$, and even $n > 3.5$ for Si) leads to total internal reflection at the interface crystal-air.

Promising advances towards improved light collection efficiency were recently demonstrated with negatively charged silicon vacancy (V_{Si}^-) centres in 4H-SiC, based on nanostructured solid-immersion lenses[14], nanopillars[15], waveguides[16], photonic crystal cavities[17], and disk resonators[18]. In most studies, nearly lifetime limited optical linewidths were observed, however, with a tendency for slow spectral wandering in nanoscopic devices. This currently prevents setting up networks of spectrally orchestrated V_{Si}^- centres in SiC.

In this work, we show a systematic investigation of V_{Si}^- centres in SiC membranes with several thicknesses ranging from 0.13 μm to 2.36 μm. Our study reveals almost no degradation of optical coherences down to membrane thicknesses of 0.7 μm, which is compatible with emitter integration into resonant enhancement structures, e.g., planar optical antennas[19] or external Fabry–Pérot cavities[20–23]. Such

[1]3rd Institute of Physics, University of Stuttgart, 70569 Stuttgart, Germany. [2]Materials Research and Technology (MRT) Department, Luxembourg Institute of Science and Technology (LIST), 4422 Belvaux, Luxembourg. [3]Department of Physics and Materials Science, University of Luxembourg, 4422 Belvaux, Luxembourg. [4]Universität des Saarlandes, Fachrichtung Physik, Campus E2.6, 66123 Saarbrücken, Germany. [5]Department of Physics, Chemistry and Biology, Linköping University, 581 83 Linköping, Sweden. [6]Leibniz-Institute of Surface Engineering (IOM), Leipzig, Germany. [7]Max Planck Institute for Solid State Research, Stuttgart, Germany. [8]These authors contributed equally: Jonah Heiler, Jonathan Körber, Erik Hesselmeier. ✉e-mail: jonathan.koerber@pi3.uni-stuttgart.de; florian.kaiser@list.lu

structures could permit to efficiently orchestrate high-quality photonic interference between multiple emitters[24]. In membranes below 0.7 μm thickness, we observe a tendency for slow spectral wandering. Also, at a 0.25 μm membrane thickness, we measure a slight linewidth broadening to ~200 MHz, which, however, is still compatible with spin-selective excitation. Thus, V_{Si}^{-} centres in SiC membranes could be used for high-fidelity electron-nuclear-spin-related experiments, such as quantum registers[25].

Results and discussion

Membrane fabrication

The steps that are used to fabricate membranes with integrated V2 centres are inspired by previous works[17,19,26], and are sketched in Fig. 1a. Our cleaning procedures in between steps are described in Supplementary Note 1. Similar to previous studies[14,16], we use electron irradiation followed by thermal annealing to create single V_{Si}^{-} centres. We note that we decided to create V2 centres before the main fabrication steps by purpose to study the influence of our fabrication on the optical properties of colour centres.

Consecutively, we remove material from the wafer side (opposite to the high-quality epilayer) by lapping until we reach a total sample thickness of ~50 μm. To remove scratches and subsurface damage induced by the lapping, a series of chemical-mechanical polishing (CMP) steps is used, yielding a total thickness of ~42 μm. Our polishing yields a root mean square (RMS) surface roughness of 2–4 Å, shown as a representative standard in the left panel of Fig. 1c and measured with an atomic force microscope (AFM) on an area of $5 \times 5\ \mu m^2$.

To create (sub-)μm-thin membranes, we use reactive-ion etching (RIE) with an SF_6-plasma at an etch-rate of 56–60 nm min^{-1}. At first, we place a diamond hard mask with 12 square openings of 350 μm length, see Supplementary Note 2 for details, on the wafer side of the sample and create trenches with a depth of ~35 μm. By using the diamond mask we retain outer frames at a thickness of ~42 μm for mechanical stability and easier handling at subsequent steps of the sample, while the 12 open regions serve as thin membranes. Consecutively, the diamond mask is removed and the sample is flipped, followed by a series of short etching steps for the final thinning. To retain control over the membrane thickness at the final etching steps, we measure the thickness minimum of each membrane, labelled as shown in Fig. 1c, with a home-built white-light-interferometer (WLI, details in Supplementary Note 3).

After the main fabrication and optical characterisation, that will be discussed in the next section, we perform a second annealing of our sample with the same parameters as the first annealing. We perform photoluminescence (PL) scans of our sample at room temperature with an excitation laser of 728 nm and 350–450 μW before the objective. We find that the background fluorescence of our sample increased by one order of magnitude after the annealing, which can be seen by comparing the upper and centre panel of Fig. 1d. Furthermore, we observe very slow bleaching of the parts of the surface that were exposed to the 728 nm laser. To clean the surface of the parasitic fluorescence, we perform a short soft-ICP etching step on the growth side of the epilayer with an SF_6-plasma. We removed ~30 nm of material, which resulted in an only slightly increased background fluorescence level compared to the one after the main fabrication, as shown in the lower panel of Fig. 1d and Supplementary Fig. 3. However, as displayed in the right panel of Fig. 1c, this soft-ICP etching induced a grain-like surface with an increase of the surface roughness by a factor of ~2.5. We suspect that the annealing step created contamination on the surface which was partially imprinted on the SiC surface at our soft-ICP step. We emphasise that the induced roughness is not related to the RIE of our main fabrication in all likelihood, since we know from previous samples that our process yields a surface roughness comparable to the one after polishing

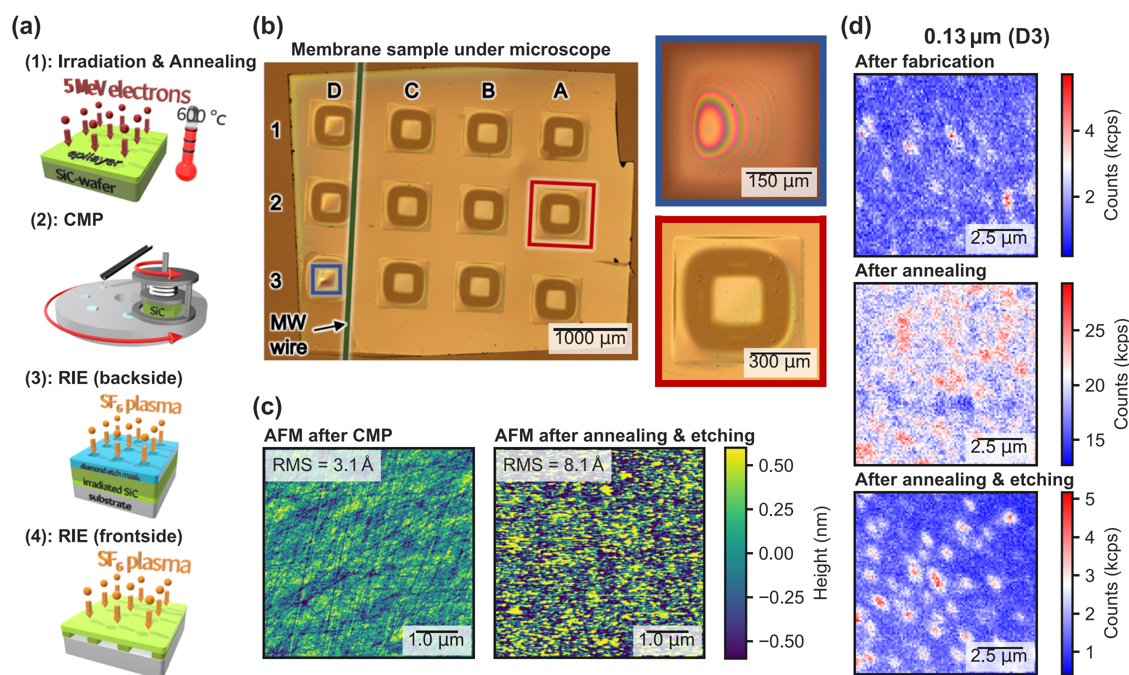

Fig. 1 | Membrane fabrication scheme and surface characterisation. a Membrane fabrication: (1) V_{Si}^{-}-creation via irradiation with electrons at an energy of 5 MeV and a dose of 2 kGy and subsequent annealing at 600 °C. (2) Lapping and CMP of the wafer down to a total sample thickness of around 40 μm. (3) Fabrication of 35 μm trenches using RIE with an SF_6-plasma. The trenches are defined by a diamond hard mask with square openings (blue). (4) Final thinning of the membranes after flipping the sample with the same RIE process already used in (3). **b** Light microscope images of the sample after fabrication. The inset with a blue frame shows a zoom of the thinnest membrane D3, where visual interference fringes indicate a thickness gradient. The red inset shows a zoom of membrane A2 with visible defects on the surface that appeared after an SF_6 soft-ICP etching that was done as part of the post fabrication. **c** Surface topography on an arbitrary position of our sample after the final polishing of step (2) (left panel) and on membrane D3 (right panel) after the post fabrication, measured with a commercial AFM. The extracted RMS-roughness are shown on the top left of each panel. **d** Photoluminescence scan under 785 nm excitation at 0.4 mW on an arbitrary position of membrane D3 after the main fabrication steps (upper), the post fabrication annealing (centre) and an additional soft-ICP etching step (lower).

(Supplementary Notes 5 and 6). After all fabrication steps, the thinnest membrane of our sample exhibits a minimum thickness of ~0.13 µm and the thickest membrane a minimum thickness of ~2.36 µm. We attribute this inhomogeneity to our lapping and polishing steps. For simplicity, we now always refer to the membrane thicknesses after the soft-ICP step.

Emission spectra in membranes and bulk

The emission spectrum of V1 (V2) centres in 4H-SiC at cryogenic temperatures is characterised by a sharp zero-phonon line (ZPL) at 862 nm (917 nm) and a broad phonon side band (PSB)[27–29]. To investigate the influence of our fabrication process on the implanted silicon vacancy centres, we record over 100 emission spectra in each of the regions. These regions comprise the only-polished bulk, the etched bulk, and the four membrane windows C1, D1, D2, and D3 with respective thicknesses of 1.54–1.66 µm, 0.58–0.63 µm, 0.63–0.72 µm, and 0.13–0.25 µm. Thicknesses were measured by WLI about 50 µm next to the respective membrane centres (see Supplementary Note 7), which corresponds to the areas in which we performed the investigations on the colour centres. Additional data for the latter two membranes can be found in Supplementary Note 8. For acquisition of spectra we developed an automatised software that optimises the focus and records a spectrum on each manually selected point of a high resolution confocal map, as shown in Fig. 2a.

Next, we extract the spectral positions of peaks in these spectra and notice that most peak positions in only polished bulk and etched bulk material align at the ZPL of the silicon vacancy centres, while the spectral positions of peaks in membranes are wide-spread over the detection window. This difference is visualised for membranes C1 and D1 in Fig. 2b. Stacking spectra with at least one peak in a two-dimensional plot results in two clear lines for V1- and V2-ZPL in the bulk case. For the membranes, however, those lines are hardly visible in this representation, indicating the fabrication process induced crystal damage in vicinity to the silicon vacancies that altered their structure and therefore their ZPL emission frequency. Motivated by this insight, we decide to continue with an annealing step (same as for the color center creation, see methods) in effort to heal the crystal and recover the altered silicon vacancy centres. Note that we only anneal the sample with membranes, while keeping the polished bulk as a reference. However, we expose both samples to a subsequent short SF_6 ICP etching step. The stacked spectra after those post-fabrication steps are depicted in the bottom row of Fig. 2b. As expected, in the bulk sample, there are essentially no observable changes. Yet, the emission spectra in the annealed membrane sample now show a significantly increased number of emission lines aligning around the typical V1- and V2-ZPL.

To quantify this change, we assign each peak in the spectra to a V1 (V2) centre if its spectral position lies maximum two spectrometer pixels, i.e. 0.7 nm, away from the position of the V1- (V2-) ZPL in bulk material. We

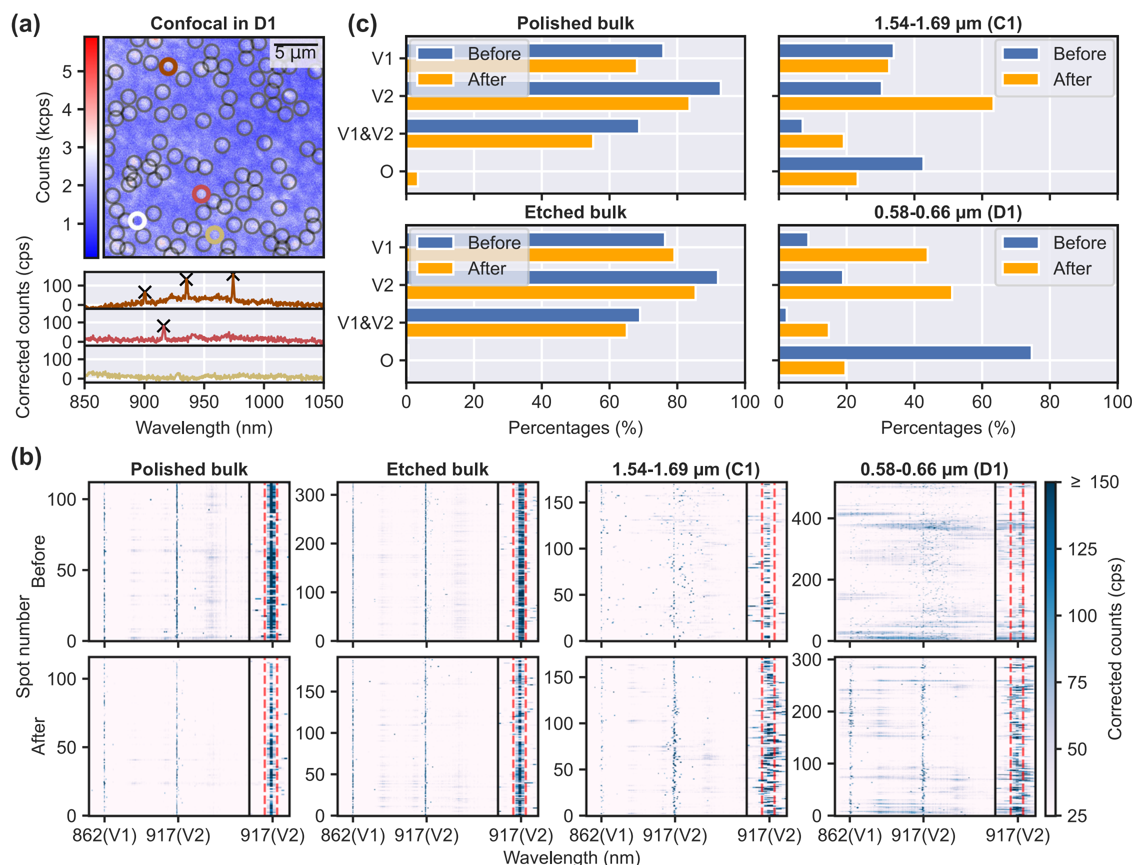

Fig. 2 | Spectra acquisition, statistics, and comparison for bulk and membrane material. **a** Confocal map of a 25 × 25 µm² region in membrane D1 with circles marking the manually selected positions of recorded photoluminescence spectra. The bold white circle indicates where the background correction spectrum was recorded, which we subtracted from all subsequent measurements. The brown, red, and yellow circles correspond to three representative spectra, which are shown below: brown/top: multiple peaks within one spectrum; red/middle: a single V2-peak; yellow/bottom: no peak. **b** Stacked photoluminescence spectra from different spots with peaks on a bulk sample that was only polished, on the bulk part of the etched membrane sample, on the membrane C1, and on the membrane D1. The upper (lower) panels show data before (after) the post-fabrication processing. Each line corresponds to a background corrected spectrum taken at one spot in the respective region. The insets on the right zoom into the wavelength interval 914–919 nm where dashed red lines indicate the region 915.7–917.1 nm in which peaks are ascribed to emission from a V2 centre for **c**. The respective membrane thickness is given in the title. Peaks in the range of 861.0–862.4 nm are considered to be V1 centres, the reasoning for these intervals is given in the main text. **c** Percentages of V1-peaks, V2-peaks, both V1- and V2-peaks (V1& V2), and unidentified peaks (O) in the spectra, obtained as in **a**, before and after the post-fabrication processing.

choose this cut-off, since we measured photoluminescence excitation (PLE) on V2 centres with ZPL peaks at most two pixel away from the bulk position. The interval for V2 centres is indicated by dashed read lines in the insets of Fig. 2b. Every peak out of both intervals is assigned to the category "other defects" (O) in the overall statistics, which is shown in Fig. 2c. This statistics also includes an extra category for simultaneous appearances of V1- and V2-peaks within a diffraction limited spot, which is a rather regular observation that we made.

Overall, the percentage occurrences show, as expected, that bulk material has the highest amount of V_{Si}^- centres at the V1- and V2-position. For membranes, after the first fabrication step, up to 74% less V1- and V2-peaks are observed, and many new emission peaks appear at different wavelengths. As a general trend, we find that the relative amount of V_{Si}^- centres decreases with reduced membrane thickness. After post-fabrication (annealing, short ICP), the amount of V_{Si}^- centres in the membranes increases up to a factor of five, indicating that some crystal damage from the fabrication was repaired. Even though the spots investigated before and after post fabrication are not exactly the same, the high number of investigated spots enables us to identify this trend. To investigate the spectral features of V2 centres in more detail, we perform additional PLE measurements.

Resonant laser excitation measurements in membranes and bulk

As depicted in Fig. 3a, we record the PLE spectra by sweeping a narrowband tunable laser across the optical transitions within the V2-peak, while detecting the PSB emission. In addition, we apply continuous microwaves (MW) at 70 MHz to mix the spin populations in the ground states, which counteracts spin-pumping processes. The MW signal is provided through a 50 μm copper wire spanned across our sample nearby the membranes D1, D2, and D3, shown in Fig. 1b. We repeat the PLE scheme $N = 20–100$ times for each emitter and different laser powers, to observe its stability over time and to get more statistics for the linewidth extraction. Four exemplary PLE scans at 2 nW excitation power in etched bulk, membrane D2, D3, and D1 are depicted in Fig 3b, c. The scan in D3 shows a significantly better signal-to-noise ratio (SNR) than the other three examples since it was recorded after post-fabrication and we upgraded our detector from an avalanche photo-diode (APD) to a superconducting nanowire single-photon detector (SNSPD) during this processing. Furthermore, the SNR reduces with smaller excitation powers, which challenges an accurate determination of the linewidths from single line scans. To obtain the linewidth from PLE scans at low SNR conditions, we need to average data over multiple scans. To additionally account for spectral wandering, we align the positions of all A_1 (A_2) peaks based on single line fits and then perform another Lorentzian fit on the sum of all single lines. From the latter fit, we extract the A_1 (A_2) linewidth as the full width at half maximum (FWHM) by converting the x-axis to frequencies based on the 1 GHz separation of the A_1 and A_2 transition[30,31]. An example of this process is shown in Fig. 3b. More details can be found in the methods section.

To be consistent with the linewidth extraction, we use this procedure for every PLE scan. Figure 3d shows averaged linewidths for different regions as a function of the resonant laser power. An overview of all extracted linewidths for individual emitters is displayed in Supplementary Note 9. The left-sided panel of Fig. 3d shows mean linewidths for 14 emitters before the post-

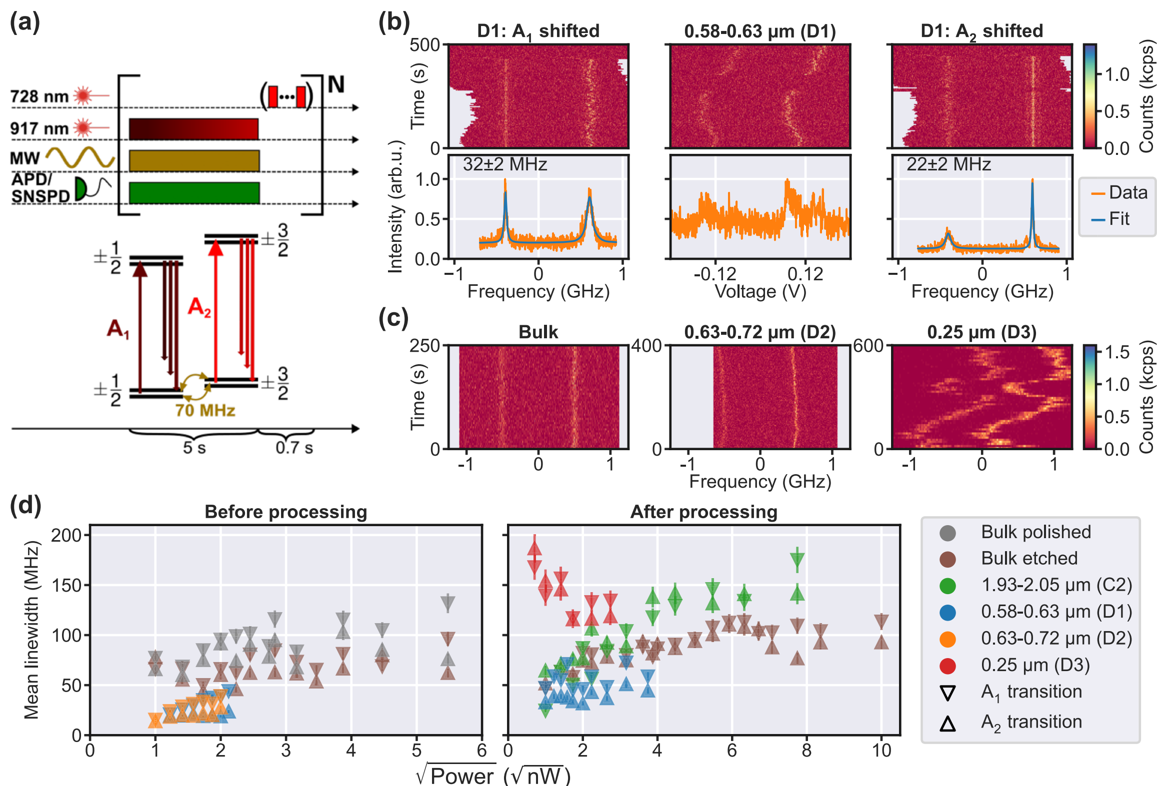

Fig. 3 | PLE measurement scheme, PLE examples with linewidth evaluation, and power dependent linewidths for membranes as well as bulk material. **a** Spin-3/2 level scheme of the V_{Si} centre together with the measurement sequence of the PLE scan in **b** consisting of $N = 100$ single line scans of 5 s each with an integration time of ~5 ms per point (see methods for details). **b** Exemplary linewidth extraction from a PLE scan of one emitter in membrane D1 at a resonant laser power of 2 nW. The middle panels show the scanned lines recorded over time and the normalised sum of all recorded lines over the applied voltage. The left (right) panels show the A_1 (A_2) shifted scanned lines and their sum over the frequency, fitted with a Lorentzian profile to extract the A_1 (A_2) linewidth. **c** PLE scans at 2 nW resonant excitation power for single emitters in the etched bulk, membrane D2, and membrane D3. The abscissa shows the frequency obtained from a conversion analogous to **b** and the respective membrane thicknesses are given in the title. **d** Mean A_1 and A_2 linewidths, extracted as in **b**, of emitters before and after post-fabrication processing in only polished bulk, etched bulk, as well as membranes C2, D1, D2, and D3 as a function of the root of the excitation power. The error bars correspond to a standard deviation of the splitting of 75 MHz (see methods section).

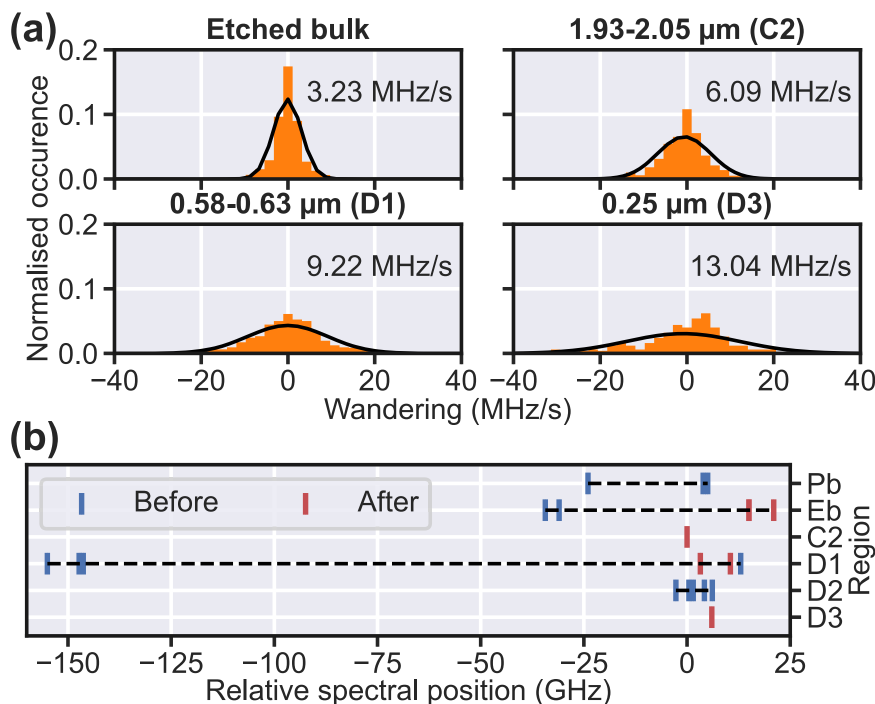

Fig. 4 | Wandering histogram and inhomogeneous distribution of the PLE positions. a Histograms of the spectral wandering in consecutive PLE lines of emitters in etched bulk material and membranes C2, D1, and D3 after the post-fabrication annealing and soft-ICP etching. The black curve represents a Gaussian distribution with the standard deviation and mean value of the wandering data. **b** Relative laser starting position for the performed PLE scans with respect to the region before and after the post-fabrication processing. The relative position of zero corresponds to an absolute frequency of 327.100 THz. Pb and Eb stand for polished bulk and etched bulk, respectively.

processing steps (annealing, short ICP), comprising 3 V_{Si} centres in the polished bulk, 2 in the etched bulk, 4 V_{Si}^- centres in membrane D1, and 5 in D2. The right-sided panel shows mean linewidths after the final processing step for 3 V_{Si}^- centres in the etched bulk and 2 in membrane D1, as well as the linewidths of 1 emitter measured in membranes C2 and D3, respectively. Although post-processing did approximately triple the amount of V2-peaks across all membranes, we found that measuring power-dependent linewidths became more difficult due to increased spectral jumping. I.e., before post-processing, we found that only 4/18~22 % of the V2 centres, for which we could observe a PLE signal, showed spectral jumps. However, after post-processing, 22/29~76 % of such V2 centres showed spectral jumping, even at low resonant laser powers (few nW). An explanation could be that annealing repaired the lattice enough to recover the original ZPL wavelengths for several V2 centres, which we have not considered before. However, these recovered V2 centres are still surrounded by some remaining lattice damage that gives rise to charge fluctuations and subsequent wavelength jumps. Since emitters in membranes are close to surfaces, it is indeed unlikely that a simple annealing step can recover a pristine quality.

The mean linewidths in the membranes D1 and D2 before the post-fabrication showed the expected tendency to slightly increase with power up to about 50 MHz at a power of 4.5 nW. They are, without exception, narrower than the mean linewidths obtained in the bulk material at the same power that go up to 132 MHz at greater powers. For a few data sets recorded at the lowest laser power, we obtain fitted linewidths slightly below the lifetime-limited values of 26 MHz (14 MHz), calculated as $(2\pi\tau)^{-1}$ from the A_1 (A_2) lifetimes $\tau = 6.1$ ns (11.3 ns)[32]. This phenomenon has been studied in detail in a previous work[33], where it was shown that measurements at low signal-to-noise can lead to an underestimation of the resonant linewidths. This is also corroborated by our studies. After the post-fabrication step, we upgraded our detectors to SNSPDs, which improved the signal-to-noise significantly. No sub-lifetime limited linewidths were recorded anymore, with the linewidths in the membrane D1 going down to 29 MHz (see section Supplementary Note 9). The linewidths in bulk material show no significant change and are similar to the linewidths in the 1.93–2.04 μm membrane C2. In the membrane D3 at 0.25 μm thickness, we measure slightly broader linewidths in the range of 116–187 MHz.

Overall, for all power series measurements, we find little or no increase of the linewidth with the optical power. This indicates that the laser powers are not yet in a regime of significant power broadening. Especially in sub-micron membranes, we observed defects to ionise more rapidly at higher laser powers, which limited our measurements to powers of $P \lesssim 10$ nW. An explanation could be a less stable charge environment for emitters in surface proximity due to an increased abundance of charge traps and/or band bending. Additionally, our data for the emitter in the thinnest membrane D3 (red triangles) shows a parasitic trend of decreased linewidths at higher excitation power. As we detail in Supplementary Note 10, this observation is explained by an increased rate of spectral jumps and ionisations at higher powers. This leads to asymmetric line shapes for which the Lorentzian fit function systematically underestimates the linewidth.

We also find that emitters in thinner membranes show an increased tendency for (slow) spectral wandering, which can be explained by the V_{Si} centre's sensitivity to electric fields and charge noise[34,35]. Qualitatively, this can be seen in Fig. 3b, c, where lines in the bulk material show no visible spectral wandering. Aligned with the membrane thickness, PLE lines show an increased wandering from membrane D2 (0.63–0.72 μm), to D1 (0.58–0.63 μm), to D3 (0.13–0.25 μm). We quantify the wandering by calculating the peak position change per time in two consecutive PLE line scans. The evaluated data is depicted in Fig. 4a in form of histograms. From the standard deviation of each data set, we see a clear correlation between an increased wandering and thinner structures, which we expect due to the closer proximity to the surface.

Lastly, we investigate the inhomogeneous distribution of our spectral PLE positions. For this purpose, we show the laser frequencies, from where we started the PLE power series in Fig. 4b. We see a distribution of 176 GHz in between all regions, with a largest contribution coming from the membrane D1 with 168 GHz. This spread can be attributed to a combination of the fabrication process and strain in the membranes and matches our observation from the emission spectra. Additionally, we observe a distribution of 29 GHz for emitters measured in the only polished bulk material, which is comparable to previous reports[16], thus confirming that deep bulk emitters are not influenced by the fabrication. This is in line with the observation that sub-surface damage is only expected within the first 2–5 μm, even before polishing[36,37].

In conclusion, we developed a reproducible method for fabrication of sub-micron 4H-SiC membranes with low surface roughness and integrated V_{Si}^- centres. As reported previously[16], we also observe a decrease in the

emitter density after the fabrication of sub-micron structures. Additionally, we showed that spectral shifts of the ZPLs induced by our initial fabrication steps can be recovered by post-processing annealing. However, the annealing process led to a reduced percentage of V_{Si}^- centres with stable PLE lines, which may require further studies on optimal post-fabrication processes. These should potentially include surface treatments to recover a pristine SiC surface quality.

All of our investigated emitters with stable PLE showed narrow linewidths below 200 MHz, which is compatible with spin-selective excitation schemes. Moreover, all emitters in the ~0.65-μm-thick membrane showed linewidths below 100 MHz, which is comparable with recent studies on V_{Si}^- centres in 4H-SiC integrated in triangular waveguides with a height of ~500 nm and a width of ~1000 nm[16], as well as ~500-nm thick disk resonators[18]. At the lowest powers, our measured linewidths in the 0.6–2-μm-thick membranes are at most 4.6 times larger than the lifetime limit (65 MHz to 14 MHz). For comparison, the linewidths of NV centres in a 3.8 μm diamond membrane, have in average a 6.6 times broadened linewidth (86 MHz to 13 MHz)[38]. Additionally, as opposed to NV centres, our V2 centres in 2-μm-thick membranes show no signs of spectral diffusion, even at high pump powers. We can also compare V2 centres in our thinnest 0.13–0.25 μm membrane to Germanium vacancy (GeV) centres in 0.11-μm-thin diamond membranes[39]. In such membranes, our V2 centres showed linewidths of ~150 MHz, which is only 6–11 times larger than the lifetime limit, depending on the used optical transition. For GeV centres, improved spectral stabilities are expected since their structural inversion symmetry isolates them from electric field fluctuations. Indeed, measurements showed an average single-scan linewidths of 95 MHz, which is ~4 times larger compared to the lifetime limited value of 26 MHz[40]. Similarly, tin-vacancy (SnV) inversion symmetry centres in diamond show very good spectral stability even below 60 nm surface proximity[41]. For an individual SnV centre in a photonic waveguide, spectral stability measurements revealed single-scan linewidths of 35 MHz. This exceeds the lifetime limit only by a factor of 1.63, even in the presence of off-resonant charge state repumping pulses. In summary, while the spectral properties of V2 centres in SiC are slightly more sensitive compared to inversion symmetry defects in diamond, they are still surprisingly robust considering the lack of inversion symmetry. At this point, we mention that this wandering can be counteracted by our previously developed resonance feedback system[16], integration of SiC colour centres into p-i-n diodes for stabilising their charge environments[42], and that we have been able to find several V_{Si}^- centres with only weak spectral wandering in our membrane D2 (0.63–0.72 μm, see Supplementary Note 11).

V_{Si}^- centres in such sub-μm-thin membranes are ideally suited for integration into tunable microcavities[43], which can significantly increase photon detection rates via emission funnelling, as well as Purcell enhancement. With the latter comes also an increase of the natural linewidths of the A_1 and A_2 optical transitions, which could mitigate spectral wandering to some extent. Higher photon detection rates will be beneficial for improving detection rates in photonic interference experiments[14], as well as improving the efficiency of the spin state readout for controlling more nuclear spin qubits[16]. Since V_{Si}^- centres can be operated without degradation of spin-optical coherences up to temperatures of $T \sim 20$ K[29], an integration into bulky microcavities imposes relatively relaxed constraints on cryogenic cooling power and management. This qualifies V_{Si}^- centres in SiC membranes as one of the prime candidates for developing quantum network architectures based on cavity-integrated solid state colour centres.

Methods

Sample growth

The sample of this study is fabricated from an a-plane, n-type 4H-SiC wafer (*Wolfspeed*). After an external polishing (*NovaSiC*) a ~10-μm-thick n-type epilayer with a free carrier concentration of $\sim 7 \times 10^{13}$ cm^{-3} is grown on the polished side along the a-axis by chemical vapour deposition. After epitaxial growth, the wafer is cut into 5×5 mm^2 pieces, and the membranes are fabricated within the epilayer of the sample.

Creation of V_{Si}^- centres

For the creation of V_{Si}^- centres we irradiate the sample with electrons at an energy of 5 MeV and a dose of 2 kGy. Subsequently, the sample is annealed for 30 min at 600 °C (temperature rise of 5℃ min^{-1}) in a ~850 mbar Ar atmosphere.

Lapping and CMP

We use a commercial CMP-tool (*PM6, Logitech*) for lapping and polishing of the wafer side. Lapping is performed with an iron plate, diamond slurry with a mean particle size of 6 μm and a plate rotation speed of 40 rpm at a pressure of 30 kPa. Typical removal rates are 7–8 μm min^{-1} for this process. The next step is a rough polishing at the same parameters as the lapping but with a polyurethane pad (*0CON-399, Logitech*) instead of the iron plate with a removal rate of ~1 μm min^{-1}. The final polishing steps are performed with a diamond slurry with a mean particle size of 0.5 μm, for one hour at a pressure of 75 kPa and for another hour with a softer pad (*0CON-387-1, Logitech*) at a pressure of 150 kPa with no measurable removal at the μm-scale. Our polishing process leads to a small thickness inhomogeneity of the resulting samples due to an edge rounding that becomes stronger with increasing polishing time (see Supplementary Note 12). This is the main reason for the different thicknesses of the individual membranes.

Reactive-ion etching

The dry etching processes we use are performed in a commercial ICP-RIE tool (*PlasmaPro80, Oxford Instruments*). It starts with a 2.5 min O_2-plasma soft-ICP cleaning step with a gas flow of 30 sccm at a pressure of 10 mTorr, an ICP power of 180 W, and a temperature of 24 °C. This step is followed by multiple 2 min SF_6-plasma etching steps with a flow of 40 sccm at 8 mTorr, an HF power of 100 W (no ICP), and a temperature of 20 °C with 2 min waiting steps in between them to prevent a significant heating of the sample. Typical etch rates for the process are 56–60 nm min^{-1}. The post-fabrication etching step consists of a 2 min SF_6 soft-ICP etching step with a gas flow of 30 sccm at a pressure of 10 mTorr, an ICP power of 250 W, and a temperature of 24 °C.

AFM measurements and evaluation

For surface characterisation we use a commercial AFM (*Veeco Dimension Icon, Veeco Instruments*) with silicon cantilevers (*Olympus OMCL-AC240TS-R3*) and measure areas of 5×5 μm^2. To deduce the RMS-surface roughness, we apply step-line corrections and a polynomial fit on the acquired raw data with the software *Gwyddion*.

Spectra measurements

We perform the spectra measurements on our sample in a *Montana Instruments* closed-cycle helium cooled cryostat at ~8 K with a home-built confocal microscope using a NA 0.9 objective with × 100 magnification and a working distance of 1 mm (*Zeiss EC Epiplan-Neofluar*). To control our hardware, we use the software package *Qudi*[44]. For acquisition of the spectra, we excite the selected spots off-resonantly with a *Toptica iBeam-Smart-CD* 728 nm laser diode and record the spectra using an *Ocean Optics NIRQuest* spectrometer with a resolution of 0.3–0.4 nm. The wavelength of the spectrometer is fine-calibrated by a tunable diode laser *Toptica DL pro* and a wavemeter *HighFinesse Angstrom WS7-60*. The peaks from the spectra are extracted using the *SciPy* method *find_peaks*.

PLE measurements

We perform the PLE measurements on the same low-temperature confocal microscope setup and use the same off-resonant repump laser as in the spectra measurements. To excite an emitter resonantly, we utilise a tunable *Toptica DL pro* laser whose light passes an acousto-optic modulator by *Gooch&Housego* operating at 270 MHz that acts as a switch. The excitation power of the laser is measured before the objective. We filter out photons emitted in the ZPL using two tunable long pass filters *Semrock TLP01-995* and detect photons in the PSB before the post-fabrication with an APD *SPCM-900-24* by *Excelitas Technologies Corp* and after the post-fabrication

with an SNSPD by *Photon Spot*. The laser frequency is monitored using a wavemeter *HighFinesse Angstrom WS7-60* and tuned by applying a voltage via a *National Instruments* data acquisition card (NIDAQ). A PLE line consists of the collected counts with respect to this applied voltage. The typical tuning range amounts to ~2 GHz around a wavelength of 917 nm. To avoid decaying into a dark state via inter-system-crossing after excitation, we drive the ground state spin transition continuously using a microwave signal at input powers of 12–15 dBm. Only in case the system ionises in a single line scan, we turn on a 728 nm laser (software-wise implemented as pulses at intervals of 1 ms for 10 μs each), to repump the system back to its negatively charged state, in the time the tunable laser returns to its starting frequency. One can determine a linewidth from a PLE scan consisting of multiple PLE lines, by summing all lines, performing a Lorentzian fit, and transforming the FWHM from voltage to frequency based on the known separation of the A_1 and A_2 transition peaks (1 GHz,[45]). However, this method only works for scans with little to no observable spectral wandering, since more than two peaks can appear in case of a stronger spectral wandering, see the middle panel of Fig. 3c. For this purpose, we have written a program that starts by trying to fit each single line scan to the sum of two Lorentzian profiles using the *SciPy* method *curve_fit* with restrains on the fit parameters, such as no negative amplitudes, FWHMs smaller than the scanned interval, manually defined limits to the peak positions, and only a small variation in the distance between the peak positions. Next, it shifts the lines where this fit was successful according to the fit parameters such that the positions of all A_1 (A_2) peaks align, sums the shifted lines and performs another Lorentzian fit. Only then is the data transformed to frequencies based on the peak splitting and the A_1 (A_2) linewidth extracted. Since a standard deviation of 75 MHz for the ZFS of the excited state was reported for V1 centres[45], and we expect a similar behaviour for V2 centres, we attribute an error of 7.5% to our extracted linewidths. The spectral wandering in the histogram in Fig. 4 stems from the peak position difference in single line fits for two consecutive lines divided by the time in between those lines. This data is converted from voltages to frequency based on the transformation value obtained as described above. We have calculated the mean errors for each evaluated region and chose the bin width to be the biggest one of these, namely 2.13 MHz s^{-1}. An insignificant amount of data points (8 out of 3471) was disregarded in the histogram, since the obtained standard deviation of the single line fits used for those points is unphysically high (>200 MHz s^{-1}).

Data availability

The data supporting the presented findings are available at the following repository: https://doi.org/10.18419/darus-3982.

Code availability

The measurement and evaluation codes used for this study are available from the corresponding author upon reasonable request.

Received: 23 August 2023; Accepted: 26 March 2024;
Published online: 04 April 2024

References

1. Awschalom, D. D., Hanson, R., Wrachtrup, J. & Zhou, B. B. Quantum technologies with optically interfaced solid-state spins. *Nat. Photonics* **12**, 516–527 (2018).
2. Bishop, S. G. et al. Enhanced light collection from a gallium nitride color center using a near index-matched solid immersion lens. *Appl. Phys. Lett.* **120**, 114001 (2022).
3. Luo, J., Geng, Y., Rana, F. & Fuchs, G. D. Room temperature optically detected magnetic resonance of single spins in GaN. *Nat. Mater.* **23**, 512–518 https://doi.org/10.1038/s41563-024-01803-5 (2024).
4. Cannon, J. K., Bishop, S. G., Hadden, J. P., Yagcí, H. B. & Bennett, A. J. Polarization study of single color centers in aluminum nitride. *Appl. Phys. Lett.* **122**, 172104 (2023).
5. Choi, S. & Aharonovich, I. Zinc Oxide Nanophotonics. *Nanophotonics* **4**, 437–458 (2015).
6. Niaouris, V. et al. Ensemble spin relaxation of shallow donor qubits in ZnO. *Phys. Rev. B* **105**, 195202 (2022).
7. Durand, A. et al. Broad Diversity of Near-Infrared Single-Photon Emitters in Silicon. *Phys. Rev. Lett.* **126**, 083602 (2021).
8. Higginbottom, D. B. et al. Optical observation of single spins in silicon. *Nature* **607**, 266 (2022).
9. Hollenbach, M. et al. Wafer-scale nanofabrication of telecom single-photon emitters in silicon. *Nat. Commun.* **13**, 7683 (2022).
10. Castelletto, S. & Boretti, A. Silicon carbide color centers for quantum applications. *J. Phys. Photonics* **2**, 022001 (2020).
11. Castelletto, S. et al. Silicon Carbide Photonics Bridging Quantum Technology. *ACS Photonics* **9**, 1434–1457 (2021).
12. Anderson, C. P. et al. Five-second coherence of a single spin with single-shot readout in silicon carbide. *Sci. Adv.* **8**, 5912 (2022).
13. Morioka, N. et al. Spin-controlled generation of indistinguishable and distinguishable photons from silicon vacancy centres in silicon carbide. *Nat. Commun.* **11**, 2516 (2020).
14. Nagy, R. et al. High-fidelity spin and optical control of single silicon-vacancy centres in silicon carbide. *Nat. Commun.* **10**, 1954 (2019).
15. Radulaski, M. et al. Scalable Quantum Photonics with Single Color Centers in Silicon Carbide. *Nano Lett.* **17**, 1782–1786 (2017).
16. Babin, C. et al. Fabrication and nanophotonic waveguide integration of silicon carbide colour centres with preserved spin-optical coherence. *Nat. Mater.* **21**, 67–73 (2022).
17. Lukin, D. M. et al. 4H-silicon-carbide-on-insulator for integrated quantum and nonlinear photonics. *Nat. Photonics* **14**, 330–334 (2020).
18. Lukin, D. M. et al. Two-Emitter Multimode Cavity Quantum Electrodynamics in Thin-Film Silicon Carbide Photonics. *Phys. Rev. X* **13**, 011005 (2023).
19. Fuchs, P., Jung, T., Kieschnick, M., Meijer, J. & Becher, C. A cavity-based optical antenna for color centers in diamond. *APL Photonics* **6**, 086102 (2021).
20. Riedel, D. et al. Deterministic enhancement of coherent photon generation from a nitrogen-vacancy center in ultrapure diamond. *Phys. Rev. X* **7**, 031040 (2017).
21. Häußler, S. et al. Diamond photonics platform based on silicon vacancy centers in a single-crystal diamond membrane and a fiber cavity. *Phys. Rev. B* **99**, 165310 (2019).
22. Salz, M. et al. Cryogenic platform for coupling color centers in diamond membranes to a fiber-based microcavity. *Appl. Phys. B* **126**, 131 (2020).
23. Ruf, M., Weaver, M. J., Van Dam, S. B. & Hanson, R. Resonant Excitation and Purcell Enhancement of Coherent Nitrogen-Vacancy Centers Coupled to a Fabry-Perot Microcavity. *Phys. Rev. Appl.* **15**, 024049 (2021).
24. Hermans, S. L. et al. Qubit teleportation between non-neighbouring nodes in a quantum network. *Nature* **605**, 663 (2022).
25. Bradley, C. E. et al. A Ten-Qubit Solid-State Spin Register with Quantum Memory up to One Minute. *Phys. Rev. X* **9**, 031045 (2019).
26. Heupel, J. et al. Fabrication and characterization of single-crystal diamond membranes for quantum photonics with tunable microcavities. *Micromachines* **11**, 1–18 (2020).
27. Wagner, M. et al. Electronic structure of the neutral silicon vacancy in 4H and 6H SiC. *Phys. Rev. B* **62**, 016555 (2000).
28. Ivády, V. et al. Identification of Si-vacancy related room-temperature qubits in 4H silicon carbide. *Phys. Rev. B* **96**, 161114 (2017).
29. Udvarhelyi, P. et al. Vibronic States and Their Effect on the Temperature and Strain Dependence of Silicon-Vacancy Qubits in 4H-SiC. *Phys. Rev. Appl.* **10**, 054017 (2020).
30. Banks, H. B. et al. Resonant Optical Spin Initialization and Readout of Single Silicon Vacancies in 4H - Si C. *Phys. Rev. Appl.* **11**, 024013 (2019).

31. Tarasenko, S. A. et al. Spin and Optical Properties of Silicon Vacancies in Silicon Carbide - A Review. *Phys. Status Solidi B* **255**, 1700258 (2018).
32. Liu, D. et al. The silicon vacancy centers in SiC: determination of intrinsic spin dynamics for integrated quantum photonics. Preprint at https://arxiv.org/abs/2307.13648v1 (2023).
33. Orphal-Kobin, L. et al. Optically Coherent Nitrogen-Vacancy Defect Centers in Diamond Nanostructures. *Phys. Rev. X* **13**, 011042 (2023).
34. Lukin, D. M. et al. Spectrally reconfigurable quantum emitters enabled by optimized fast modulation. *Npj Quantum Inf.* **6**, 80 (2020).
35. Rühl, M., Bergmann, L., Krieger, M. & Weber, H. B. Stark Tuning of the Silicon Vacancy in Silicon Carbide. *Nano Lett.* **20**, 658–663 (2020).
36. Geng, W. et al. Identification of subsurface damage of 4H-SiC wafers by combining photo-chemical etching and molten-alkali etching. *J. Semicond.* **43**, 102801 (2022).
37. Wang, W. et al. Chemical-Mechanical Polishing of 4H Silicon Carbide Wafers. *Adv. Mater. Interfaces* **10**, 2202369 (2023).
38. Ruf, M. et al. Optically Coherent Nitrogen-Vacancy Centers in Micrometer-Thin Etched Diamond Membranes. *Nano Lett.* **19**, 3987–3992 (2019).
39. Guo, X. et al. Tunable and Transferable Diamond Membranes for Integrated Quantum Technologies. *Nano Lett.* **21**, 10392–10399 (2021).
40. Bhaskar, M. K. et al. Quantum Nonlinear Optics with a Germanium-Vacancy Color Center in a Nanoscale Diamond Waveguide. *Phys. Rev. Lett.* **118**, 223603 (2017).
41. Arjona Martínez, J. et al. Photonic Indistinguishability of the Tin-Vacancy Center in Nanostructured Diamond. *Phys. Rev. Lett.* **129**, 173603 (2022).
42. Anderson, C. P. et al. Electrical and optical control of single spins integrated in scalable semiconductor devices. *Science* **366**, 1225–1230 (2019).
43. Körber, J. et al. Scanning Cavity Microscopy of a Single-Crystal Diamond Membrane. *Phys. Rev. Appl.* **19**, 064057 (2023).
44. Binder, J. M. et al. Qudi: A modular python suite for experiment control and data processing. *SoftwareX* **6**, 85–90 (2017).
45. Nagy, R. et al. Narrow inhomogeneous distribution of spin-active emitters in silicon carbide. *Appl. Phys. Lett.* **118**, 144003 (2021).

Acknowledgements

We acknowledge fruitful discussions with Dr. Daniil Lukin, Dr. Melissa Guidry, Dr. Julia Heupel, Dr. Roman Kolesov, Vladislav Bushmakin, and Marcel Krumrein, experimental help from Arnold Weible and Ole Sumpf as well as assistance in proof-reading of the manuscript from Raphael Wörnle. J.H., F.K., and J.W. acknowledge support from the European Commission for the Quantum Technology Flagship project QIA (Grant agreements No. 101080128, and 101102140). P.K., F.K., J.U.H, and J.W. acknowledge support from the European Commission through the QuantERA project InQuRe (Grant agreements No. 731473, and 101017733). P.K., F.K. and J.W. acknowledge the German ministry of education and research for the project InQuRe (BMBF, Grant agreement No. 16KIS1639K). C.B., F.K. and J.W. further acknowledge the German ministry of education and research for the project QR.X (BMBF, Grant agreements No. 16KISQ001K and 16KISQ013), while J.W. also acknowledges support for the project Spinning (BMBF, Grant agreement No. 13N16219). F.K. and J.W. additionally acknowledge the Baden-Württemberg Stiftung for the project SPOC (Grant agreement No. QT-6). F.K. acknowledges funding by the Luxembourg National Research Fund (FNR, project: 17792569) in addition. J.U.H further acknowledges support from the Swedish Research Council under VR Grant No. 2020-05444 and Knut and Alice Wallenberg Foundation (Grant No. KAW 2018.0071).

Author contributions

J.H., J.K., and E.H. contributed equally to this work. The project was conceived by J.H., J.K., P.F., C.B., and F.K. and supervised by F.K. and J.W. The high-quality epilayer was grown by J.U.H. and M.G. and the sample was electron irradiated by W.K. J.H., J.K., R.S., and P.F. have been involved in the fabrication and related measurements of all shown samples. The optical setups were constructed by J.H., J.K., E.H., P.K., P.F., and F.K. The optical measurements were conducted by J.H., E.H., and P.K. and analysed by J.H., J.K., E.H., and F.K. The manuscript was written by J.H., J.K., and F.K. All authors contributed to the manuscript.

Funding

Open Access funding enabled and organized by Projekt DEAL.

Competing interests

The authors declare no competing interests.

Additional information

Supplementary information The online version contains supplementary material available at https://doi.org/10.1038/s41535-024-00644-4.

Correspondence and requests for materials should be addressed to Jonathan Körber or Florian Kaiser.

Reprints and permissions information is available at http://www.nature.com/reprints

Publisher's note Springer Nature remains neutral with regard to jurisdictional claims in published maps and institutional affiliations.

Open Access This article is licensed under a Creative Commons Attribution 4.0 International License, which permits use, sharing, adaptation, distribution and reproduction in any medium or format, as long as you give appropriate credit to the original author(s) and the source, provide a link to the Creative Commons licence, and indicate if changes were made. The images or other third party material in this article are included in the article's Creative Commons licence, unless indicated otherwise in a credit line to the material. If material is not included in the article's Creative Commons licence and your intended use is not permitted by statutory regulation or exceeds the permitted use, you will need to obtain permission directly from the copyright holder. To view a copy of this licence, visit http://creativecommons.org/licenses/by/4.0/.

© The Author(s) 2024, corrected publication 2024